Cytoskeleton integrity influences XRCC1 and PCNA dynamics at DNA damage

Verena Hurst[a,b], Kiran Challa[a], Kenji Shimada[a], and Susan M. Gasser[a,b,*]
[a]Friedrich Miescher Institute for Biomedical Research, CH-4058 Basel, Switzerland; [b]Faculty of Natural Sciences, University of Basel, CH-4056 Basel, Switzerland

ABSTRACT **On induction of DNA damage with 405-nm laser light, proteins involved in base excision repair (BER) are recruited to DNA lesions. We find that the dynamics of factors typical of either short-patch (XRCC1) or long-patch (PCNA) BER are altered by chemicals that perturb actin or tubulin polymerization in human cells. Whereas the destabilization of actin filaments by latrunculin B, cytochalasin B, or Jasplakinolide decreases BER factor accumulation at laser-induced damage, inhibition of tubulin polymerization by nocodazole increases it. We detect no recruitment of actin to sites of laser-induced DNA damage, yet the depolymerization of cytoplasmic actin filaments elevates both actin and tubulin signals in the nucleus. While published evidence suggested a positive role for F-actin in double-strand break repair in mammals, the enrichment of actin in budding yeast nuclei interferes with BER, augmenting sensitivity to Zeocin. Our quantitative imaging results suggest that the depolymerization of cytoplasmic actin may compromise BER efficiency in mammals not only due to elevated levels of nuclear actin but also of tubulin, linking cytoskeletal integrity to BER.**

Monitoring Editor
Kerry Bloom
University of North Carolina, Chapel Hill

Received: Nov 2, 2020
Revised: Aug 3, 2021
Accepted: Aug 4, 2021

INTRODUCTION

The cytoskeleton is an evolutionary conserved network containing three filament types, which enable cells to maintain their shape, move, divide, respond to mechanical stress, and perform intracellular transport (Pollard and Goldman, 2018). While intermediate filaments self-assemble, the polymerization of actin and tubulin (microtubule) filaments requires energy and is regulated on multiple levels (Pollard and Goldman, 2018). Importantly, actin and tubulin networks are interlinked (Mohan and John, 2015; Pimm and Henty-Ridilla, 2021). Moreover, actin and/or microtubule cytoskeletons are connected to the nuclear lamina, an intermediate filament network that subtends the nuclear envelope, through a multiprotein LINC complex that spans the nuclear membrane and influences DNA position (Chang *et al.*, 2015; Kim *et al.*, 2015). In parallel to this physical connection between filamentous networks in the cytoplasm and nucleus, mono- or dimeric forms of actin and tubulin shuttle between the two compartments (Walss-Bass *et al.*, 2002; Stuven *et al.*, 2003; Akoumianaki *et al.*, 2009; Dopie *et al.*, 2012; Hendzel, 2014; Schwarzerova *et al.*, 2019). Globular actin paired with actin-related proteins also form an integral part of nucleosome remodeling and histone acetylation complexes (e.g., BAF, INO80, SRCAP, and TIP60), which regulate genome accessibility (Seeber *et al.*, 2013; Kapoor and Shen, 2014; Hurst *et al.*, 2019).

Both globular (G) and filamentous (F) forms of actin have been implicated in nuclear processes, such as DNA repair (Belin *et al.*, 2015; Caridi *et al.*, 2019; Hurst *et al.*, 2019) and transcription (Dopie *et al.*, 2012; Serebryannyy *et al.*, 2016; Wei *et al.*, 2020). Whereas data from *Drosophila* and mammalian cells argue for a positive role of nuclear actin filaments in homology-directed repair and nonhomologous end joining (NHEJ) (Andrin *et al.*, 2012; Caridi *et al.*, 2018; Schrank *et al.*, 2018), other evidence suggests that the appearance of stable actin filaments in the nucleus is either

This article was published online ahead of print in MBoC in Press (http://www.molbiolcell.org/cgi/doi/10.1091/mbc.E20-10-0680).

Declaration of interest: The authors declare no competing financial interests.

Author contributions: V.H. wrote the manuscript, performed experiments, and analyzed the data; K.C. performed experiments; K.S. and S.M.G. analyzed the data and edited the manuscript.

ORCID: Verena Hurst (0000-0002-8521-1899); Kiran Challa (0000-0001-7141-1841); Kenji Shimada (0000-0002-6670-3118); Susan M Gasser (0000-0003-3610-9123). Website: www.fmi.ch.

*Address correspondence to: Susan M. Gasser (susan.gasser@fmi.ch).

Abbreviations used: BER, base excision repair; BSA, bovine serum albumin; CytB, cytochalasin B; FCS, fetal calf serum; FRAP, fluorescence recovery after photobleaching; HRP, horseradish peroxidase; Jasp, jasplakinolide; LatA, latrunculin A; LatB, latrunculin B; MIP, maximum intensity projection; NHEJ, nonhomologous end joining; Noc, nocodazole; PBS, phosphate-buffered saline; PCNA, proliferating cell nuclear antigen; PFA, paraformaldehyde; RT, room temperature.

disease-linked or stress-induced (Serebryannyy *et al.*, 2016). In budding yeast, the loss of cytoplasmic actin filament integrity and/or increased levels of nuclear actin compromises base excision repair (BER; Shimada *et al.*, 2020). This led us to study the impact of altered actin filament structure in the context of BER in mammalian cells.

BER acts on damage arising from base oxidation, alkylation, and deamination, triggered from endogenous as well as exogenous conditions at the rate of 40,000 to 50,000 lesions per day (Lindahl, 1993; Krokan and Bjoras, 2013). Repair is initiated by excising a damaged or oxidized base (for instance, 8-oxo-guanine) leaving a gap that is repaired by replacement with an undamaged nucleotide (Dianov and Hubscher, 2013). Depending on the number of nucleotides replaced, BER is divided into short-patch (usually one nucleotide) and long-patch BER (multiple nucleotides) (Beard *et al.*, 2019). Each pathway involves multiple steps and a variety of enzymes that work in short-lived complexes (Howard and Wilson, 2018; Moor and Lavrik, 2018; Endutkin *et al.*, 2019; Steinacher *et al.*, 2019).

In brief, BER is initiated by the excision of the damaged base by a lesion-specific DNA glycosylase, generating an abasic site (Krokan and Bjoras, 2013; Beard *et al.*, 2019). The DNA strand containing the abasic site is then cleaved by AP-endonuclease 1 (APE1) generating a 3′-OH (hydroxyl) and a 5′-dRP (deoxyribose phosphate) and exposing a base on the nonlesion strand that serves as a template for DNA polymerase elongation (Beard *et al.*, 2019). PARP-1 [poly (ADP-ribose) polymerase 1] and XRCC1 (x-ray repair cross-complementing 1), two accessory factors, bind the gap to promote repair by DNA polymerases β or λ, which remove the 5′-dRP. The filled gap is then sealed by ligase III (Beard *et al.*, 2019). In long-patch BER, DNA polymerase β, δ, or ε work with PCNA (proliferating cell nuclear antigen) to synthesize a new DNA strand that displaces the lesion, generating a 5′ overhang that is excised by flap endonuclease 1, FEN1 (Beard *et al.*, 2019). The remaining nick is sealed by DNA ligase I. Although PCNA is involved in long-patch BER, it is also integral to genomic replication and to other repair processes that involve DNA pol δ or ε, such as nucleotide excision pathways (Nichols and Sancar, 1992) and DNA mismatch repair (Umar *et al.*, 1996).

Work from our lab in budding yeast has shown that depolymerization of the actin cytoskeleton inhibits the repair of Zeocin-induced damage by BER resulting in massive chromosome fragmentation (Shimada *et al.*, 2013, 2020). Although we did not detect massive genome fragmentation in mammalian cells under the same conditions, we observed synergistic inhibition of cell proliferation when Zeocin and actin depolymerizing agents are combined, as well as a latrunculin dose-dependent increase in DNA damage checkpoint signaling in primary human fibroblasts (Hurst *et al.*, unpublished data). Here we have examined the impact of cytoskeletal perturbation on BER factors in mammalian cells.

RESULTS AND DISCUSSION

Nuclear actin levels are not changed on Zeocin-induced damage

Zeocin is a DNA-nicking and base-modifying agent that triggers single- and double-strand breaks in a 9:1 ratio (Povirk, 1996); thus, Zeocin-induced lesions are primarily repaired by BER. Because of synergy detected between reagents that depolymerize actin filaments [e.g., latrunculin A (LatA) or latrunculin B (LatB)] and Zeocin in both yeast and mammalian cells (Shimada *et al.*, 2013; Supplemental Figure S1a), we checked whether the actin cytoskeleton showed morphological changes, or if actin shifted toward the nucleus, in response to Zeocin in the absence and presence of LatA. We treated HeLa cells with either Zeocin alone or LatA + Zeocin (Figure 1a) and also monitored the effects of a Zeocin titration together with LatA in U2OS cells (Figure 1b). In U2OS cells F-actin is detected by staining with rhodamine-linked phalloidin, while in HeLa cells we used endogenously expressed nuclear probes that bind G- or F-actin.

We first confirmed that low levels of Zeocin elicit DNA damage in the absence and presence of LatA, as monitored by Histone H2AX phosphorylation (Supplemental Figure S1, b and c) and the appearance of γH2AX foci (Supplemental Figure S1d). This is true in HeLa cells, in U2OS cells, and in primary human fibroblasts (HDFn). The treatment of cells with Zeocin alone did not visibly alter the actin cytoskeleton based on phalloidin staining (Figures 1a and 2; Hurst *et al.*, unpublished data), nor was actin detected at laser-induced damage as monitored by a G- and F-actin-binding probe in living cells (Supplemental Video S1). LatA, on the other hand, clearly compromised cytoplasmic actin filaments, creating bright perinuclear aggregates of actin as well as elevated nuclear actin signal, particularly in U2OS cells (Figure 1b). By quantifying the ratio of nuclear over cytoplasmic F-actin on phalloidin-stained cells (Figure 1c), we see a significant increase in nuclear actin on LatA, which persists as Zeocin levels increase from 0 to 100 μg/ml (Figure 1c). In U2OS cells, 50 μg/ml Zeocin was sufficient to trigger a significant increase in foci containing XRCC1, a key player in short-patch BER, both in the presence and in the absence of LatB, a latrunculin closely related to LatA with a similar mode of action (Supplemental Figure S1e; Low *et al.*, 1975; Spector *et al.*, 1989; Wakatsuki *et al.*, 2001).

Because phalloidin only recognizes filamentous actin, we also investigated actin following incubation with Zeo or Zeo + LatA using endogenously expressed nuclear G- and F-actin probes. These probes consist of eGFP-NLS fused with either the G-actin-binding domain of MAL/MKL1 (RPEL-1-EN), or the F-actin-binding domain of utrophin (Utr230), as previously described (Belin *et al.*, 2015). For a control we use eGFP-NLS alone, which shows diffuse nuclear signals with bright nucleolar localization (Figure 1a). We did not observe any change for the nuclear G-actin probe RPEL1-EN on Zeocin treatment ± LatA, and the nucleolar signal resembled that of GFP-NLS (Figure 1a). In cells expressing Utr230-EN, which is a high-affinity, nuclear-localized F-actin binder, we observed a strong diffuse nuclear signal after Zeocin exposure (an example is shown in Figure 1a). In contrast to another study (Belin *et al.*, 2015), we found that the formation of damage-induced nuclear actin structures such as stable nuclear actin rods or filaments was extremely rare, even in the presence of Utr230-EN. We scored these in <10% of the cells treated with both Zeocin and LatA. Their low frequency and dependence on an actin polymerization inhibitor suggests that they are either transient or pathological phenomena, which may occur in rare "jackpot" cells that have high levels of both DNA damage and Utr230EN (see arrow, Figure 1a). Equally rare are cells that incur large numbers of XRCC1 foci following Zeocin treatment (Supplemental Figure S1e), supporting the idea that some cells are particularly vulnerable to Zeocin damage. We propose that damage-correlated nuclear actin filaments are nucleated by the F-actin probe (Utr230EN) itself, as discussed elsewhere (Du *et al.*, 2015; Hurst *et al.*, 2019). The strong affinity of Utr230EN for actin (Galkin *et al.*, 2002; Moores and Kendrick-Jones, 2000) renders it able to concentrate actin sufficiently to favor polymerization, particularly when cytoplasmic filaments are destabilized. Indeed, the depolymerization of the actin cytoskeleton may lead to exceptionally high levels of nuclear actin. Overall, our most noteworthy finding is that latrunculin is responsible for the increase in nuclear actin and not damage arising from Zeocin alone (Figure 1).

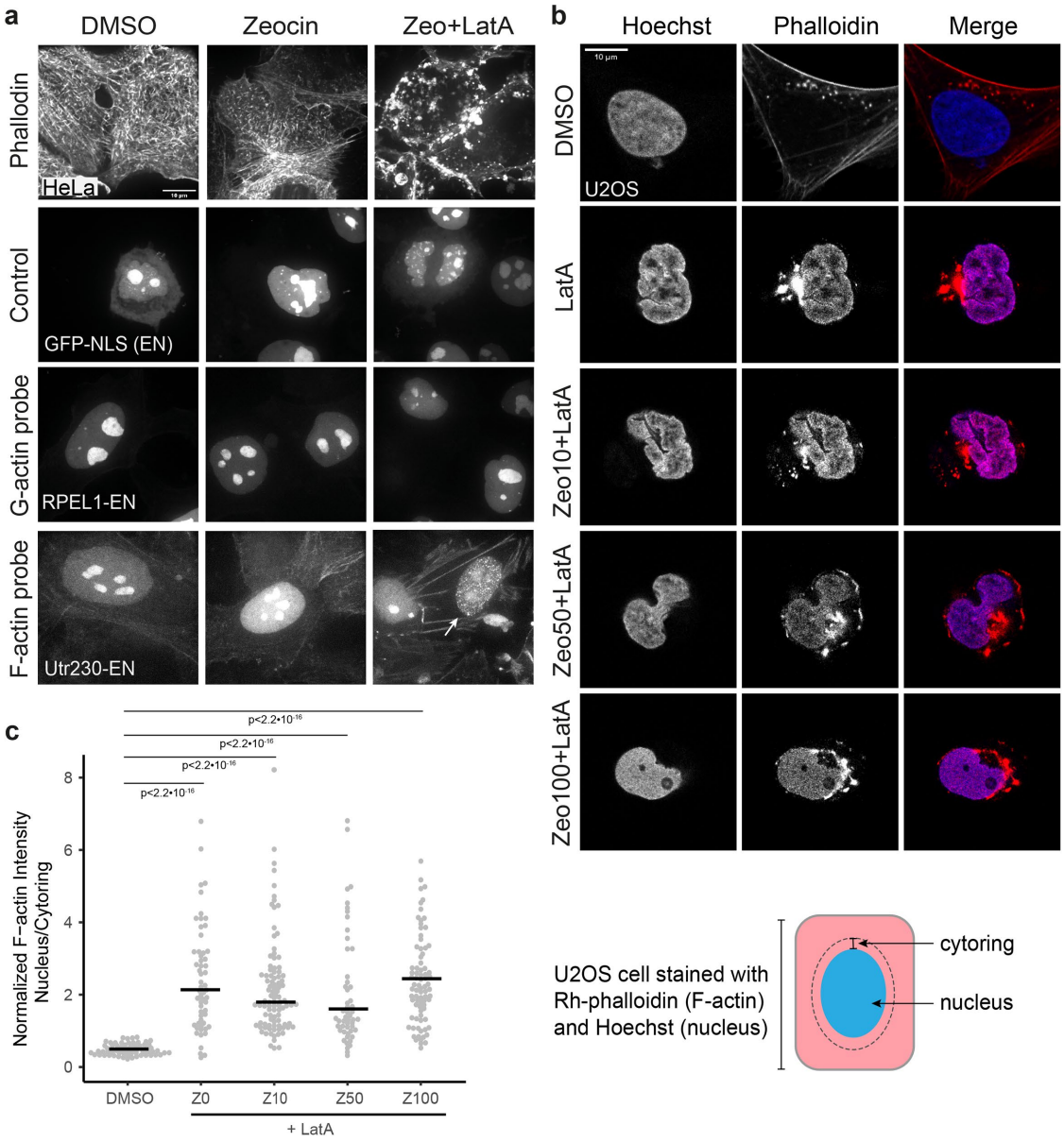

FIGURE 1: Zeocin and LatA do not cause visible synergistic actin changes. (a) HeLa cells expressing probes for nuclear G-actin (RPEL1-EN), F-actin (Utr230-EN), or eGFP-NLS (EN) as a control construct were treated with 50 µg/ml Zeocin or a combination of Zeocin and 300 nM LatA for 1 h prior to fixation and confocal image acquisition. Cells expressing those constructs were compared with native cells stained with Rh-phalloidin postfixation. F-actin (Utr230-EN) expressing cells were counterstained with phalloidin (see weak cytoskeletal background fluorescence). A jackpot cell is indicated with an arrow. The images show maximum projections of image Z-stacks. Scale bar = 10 µm for all images. (b) U2OS cells were treated with DMSO, 300 nM LatA, or a combination of 300 nM LatA plus 10, 50, or 100 µg/ml Zeocin for 45 min. Cells were fixed and stained with Hoechst (nucleus, blue) and Rh-phalloidin (F-actin, red) prior to confocal image acquisition. Images shown are the central plane of the acquired image Z-stack, and the central plane was used for quantitation. Scale bar = 10 µm for all images. (c) Quantitation of the image data set of which selected examples are shown in panel b, according to the scheme to the right, indicating the cytoring area around the nucleus. The cytoring width of 10 pixels was used to calculate the nucleus/cytoring F-actin intensity ratio determined in the red channel (Rh-phalloidin). Each dot represents this ratio in one cell ($N \geq 52$ per condition). Horizontal bars indicate median values. Conditions were compared with a Wilcoxon rank sum test in R. Relevant p values are indicated.

Immunostaining visualizes cytoplasmic APE1 accumulation

When combined, Zeocin and latrunculin lead to increased cell death (Supplemental Figure S1a). Assuming that failure to repair DNA precedes cell death, we asked whether Zeocin, LatB, or a combination of both alters repair factor localization. To this end, we imaged APE1, the key single-strand nick-generating endonuclease acting during BER. In Cos7 cells stably expressing APE1-GFP, the endonuclease is present in both the nucleus and the cytoplasm. Its localization does not change visibly on treatment with either Zeocin or LatB, although the cells clearly respond to the latter, becoming less flat and extended (Supplemental Figure S1f). Zeocin alone does not affect cell morphology (Supplemental Figure S1f). Whereas live

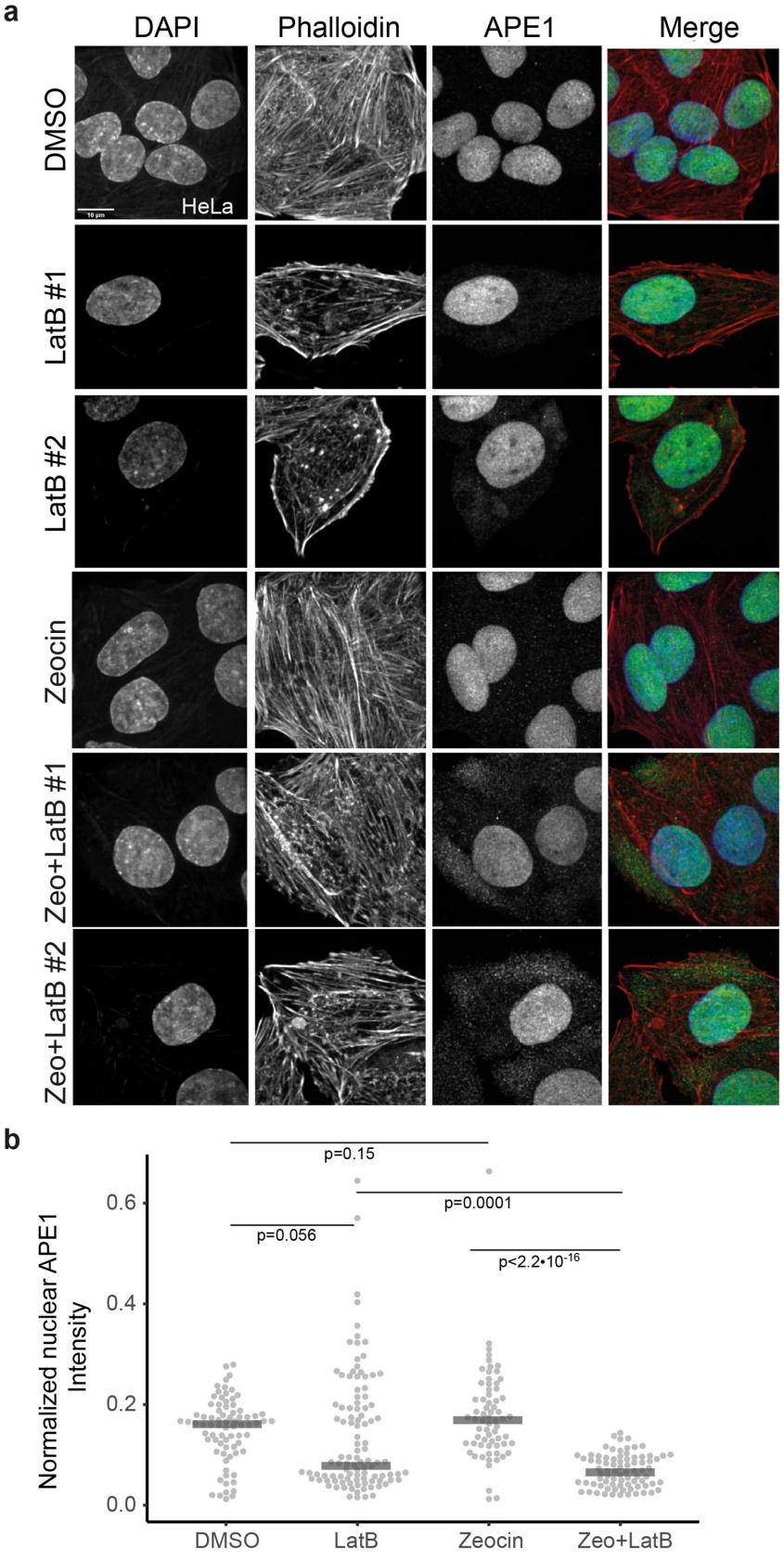

FIGURE 2: LatB increases the insoluble cytoplasmic APE1 signal. (a) HeLa cells were exposed to 300 nM LatB or to 50 µg/ml Zeocin, or a combination of both for 1 h. Cells were fixed and subjected to immunofluorescent staining with anti-APE1 (visualized in green), DNA staining with DAPI (blue) and an F-actin staining with Rh-phalloidin (red). Images show maximum intensity projections (MIPs) and independent fields are labeled #1 and #2. Scale bar = 10 µm. (b) Quantitation of the image data set for which selected examples are shown in a. Each dot represents the nuclear average APE1 pixel intensity ($N \geq 67$ per condition). Intensities were measured within a DAPI mask (nucleus) on average intensity projections of image Z-stacks in the green channel. Bars indicate median values and columns were compared with a Wilcoxon test in R. Relevant p values are indicated in the graph; for Zeo vs. DMSO, $p = 0.145$ (not significant).

imaging of APE1-GFP cannot distinguish bound from soluble fractions of the enzyme, immunostaining allows the soluble fraction to be washed away after fixation, enabling one to quantify DNA-bound APE1. In HeLa cells exposed to DMSO only, immunostaining showed APE1 highly enriched in the nucleus with the cytosolic fraction barely detected (Figure 2a). However, actin depolymerization (LatB) led to an increase in cytoplasmic APE1, at least in the presence of Zeocin, as indicated by the median values of the average nuclear APE1 fluorescence (Figure 2b). Indeed, we see a significant LatB-induced decrease in nuclear APE1 following exposure to Zeocin (Figure 2b) and an increase in weak cytoplasmic APE1 puncta on Zeocin and LatB (Figure 2a). The latter likely reflects APE1 engagement in mitochondrial repair events (Chattopadhyay *et al.*, 2006). Overall, this suggests that rather than affecting APE1 nuclear accumulation, LatB and Zeocin together trigger an increase in insoluble cytoplasmic APE1, consistent with an increase in mitochondrial DNA damage (Chattopadhyay *et al.*, 2006).

Quantitation of XRCC1 and PCNA at laser-induced damage

To obtain subnuclear resolution of the nuclear BER response, we turned to an imaging regime that measures BER factor accumulation at laser-induced lesions. Using live microscopy, we investigated the recruitment of GFP-tagged XRCC1 or PCNA to BER lesions in U2OS cells (Figure 3a). The two tagged proteins are differentially involved in short-patch (XRCC1) and long-patch (PCNA) BER pathways, respectively (Figure 3b), and have been used previously to study repair kinetics (Schuermann *et al.*, 2020). Instead of Zeocin, which yields variable numbers of XRCC1 foci (Supplemental Figure S1d), we monitored the dynamics of GFP-tagged PCNA or XRCC1 to laser-induced damage using a 405-nm laser to induce a line of DNA damage in living U2OS cells (Godon *et al.*, 2008; Miura, 1999; Muster *et al.*, 2017; Schuermann *et al.*, 2020). The GFP dynamics following laser microirradiation are tracked over time and the intensity for each time point reflects repair factor density at the lesion (Figure 3c).

Quantitation of GFP intensities at the laser line for 2 min showed that the saturation of XRCC1 at damage is reached more rapidly than that of

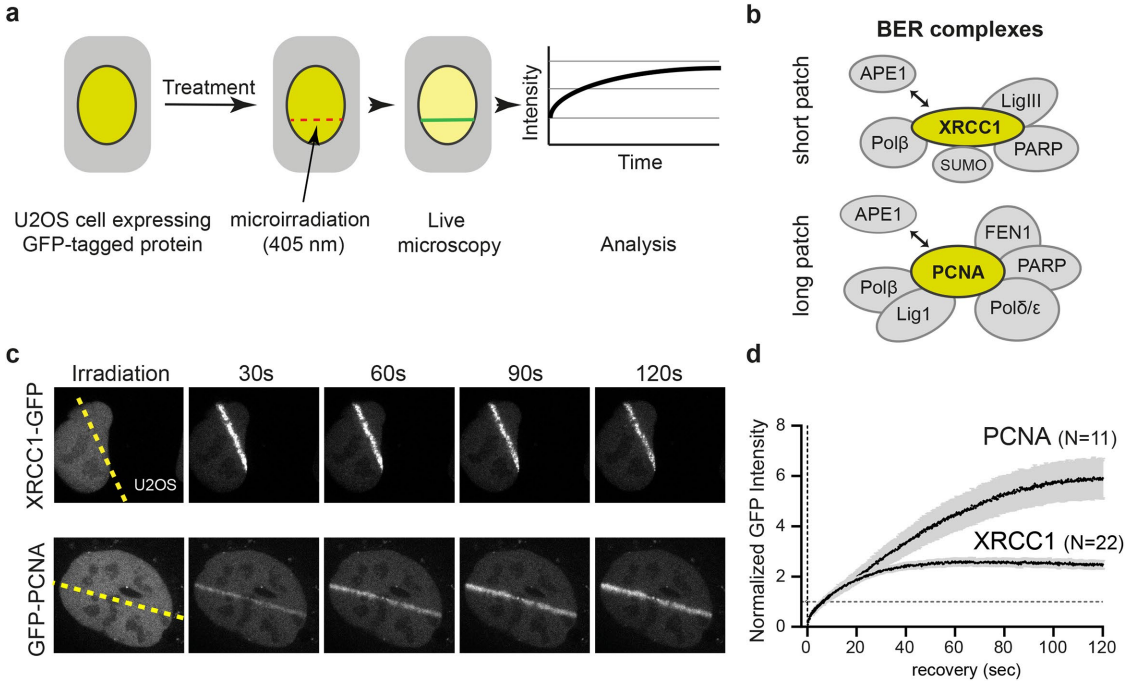

FIGURE 3: BER factors XRCC1 and PCNA are recruited to laser-induced DNA damage. (a) Experimental flow of the laser-induced damage BER factor recruitment assay. Cells expressing GFP-tagged XRCC1 or GFP-tagged PCNA are subjected to either actin or tubulin perturbation by drug treatment prior to imaging. Thereafter DNA damage is induced with a 405-nm laser and factor recruitment is measured over time. The normalized intensity at the laser line is plotted. Note that absolute intensities are different for each factor studied. (b) Composition of BER complexes containing XRCC1 and PCNA (Steinacher *et al.*, 2019). Two types of BER, namely, long-patch and short-patch, are carried out by partially overlapping subsets of proteins. Long-patch BER replaces a long stretch of nucleotides and uses PCNA and a replicative polymerase (DNA pol δ or pol ε). Short-patch BER uses uniquely XRCC1, DNA Pol β, and Ligase III. Upstream of both is the creation of an endonucleolytic cleavage by APE1, which precedes glycolytic removal of a damaged base. APE1 is not as tightly bound, whereas the other components come in stable complex regulated by sumoylation (Steinacher *et al.*, 2019). (c) Recruitment kinetics of XRCC1 and PCNA are different. Examples of confocal images from a time series showing the recruitment of XRCC1-GFP or GFP-PCNA to sites of DNA damage along a laser line (dotted yellow line) in U2OS cell nuclei. Selected frames demonstrate the dynamics over 2 min. (d) Quantitation of the image time series for which examples are shown in c. The GFP intensity at the site of laser-induced DNA damage was normalized in each image of the series to the GFP intensity outside the laser line. The normalized intensity was calibrated by setting the pre laser intensity to 1. The quantitation averages data from 22 cells for XRCC1-GFP and 11 cells for GFP-PCNA.

PCNA, consistent with the preference for rapid short-patch repair over long-patch repair in mammalian BER (Figure 3, c and d). We estimate that it took 40 s for XRCC1 to reach its plateau and nearly 100 s for PCNA (Figure 3, c and d). These values are similar to rates published for S-phase cells (50 s for XRCC1 and 80 s for PCNA) (Godon *et al.*, 2008). Over a population of cells, PCNA levels are higher, perhaps due to the more rapid turnover of XRCC1 and/or the involvement of PCNA in other repair events (Figure 3, c and d). It was expected that the two factors would respond with different kinetics and show different normalized intensities, as there are differences in protein abundance, size, function, and binding properties, as well as their cofactors and roles in repair.

Actin perturbation decreased the accumulation of XRCC1 at laser-induced damage

Given the proposed impact of actin on repair, we next tested BER factor recruitment following the perturbation of actin using drugs that inhibit actin polymerization, namely, LatB or cytochalasin B (CytB) (Low *et al.*, 1975; Spector *et al.*, 1989; Wakatsuki *et al.*, 2001), as well as jasplakinolide (Jasp), which stabilizes actin filaments (Holzinger, 2009; Visegrady *et al.*, 2005). We find that the treatment with any of these actin-modulating drugs decreased the intensity of the XRCC1 signal at the laser line (Figure 4a), whereas PCNA accumulation was not altered (Figure 4b). While actin or actin-binding factors have been implicated in mammalian DSB repair (Belin *et al.*, 2015; Caridi *et al.*, 2018; Schrank *et al.*, 2018), this is the first report indicating that the perturbation of actin filament formation might impact mammalian BER. Here perturbation of the actin cytoskeleton appears to decrease BER factor accumulation. Our observations parallel those of an earlier study that tracked the recruitment to the 405-nm laser-induced damage of KU80-GFP, a factor involved in NHEJ. The authors observed a persistent retention of KU80 at damage that was reduced by actin perturbation either by CytD or by expression of a polymerization-incompetent nuclear-targeted mutant form of actin (G13R) (Andrin *et al.*, 2012). The authors proposed that F-actin actively stabilizes the KU heterodimer at the break site (Andrin *et al.*, 2012), which could reflect either enhanced recruitment or delayed repair and release.

To see if the effect of actin-filament inhibition might be due to actin at the laser-induced damage, we induced a line of damage in

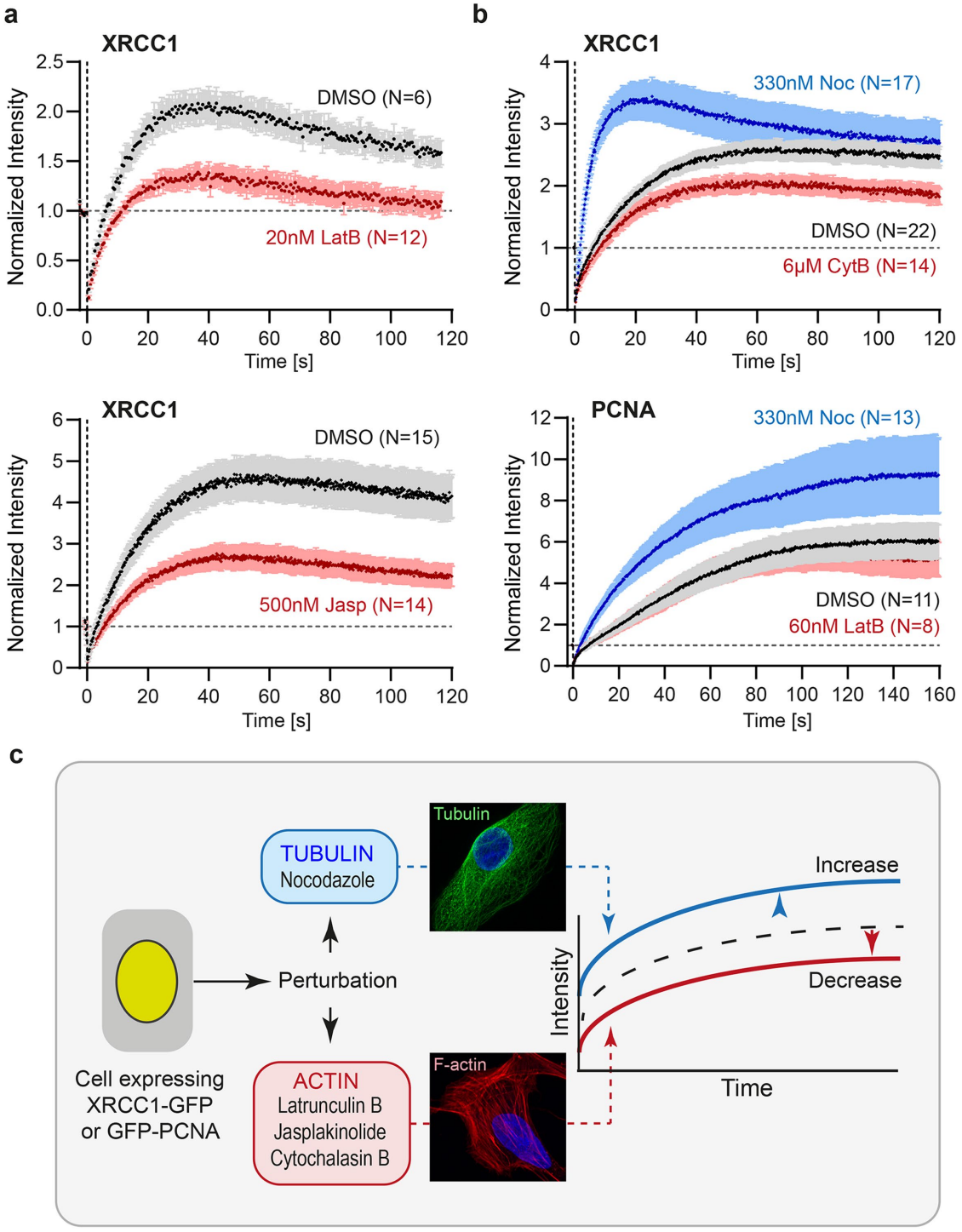

FIGURE 4: Cytoskeletal integrity alters the transient accumulation of XRCC1 and PCNA at laser-induced damage. (a) Results of image quantitation of GFP-XRCC1 accumulation as illustrated in Figure 3a and described in *Materials and Methods*. (b) As panel a, except XRCC1 is measured in the upper graph and GFP-PCNA in the lower graph. In both cases, U2OS cells were treated with 20–60 nM LatB, 500 nM Jasp, 6 μM CytB, or 330 nM Noc, as indicated for 30 min prior to laser irradiation and confocal image acquisition. Actin perturbing drugs LatB, Jasp, and CytB decrease XRCC1 accumulation at the site of DNA damage, while microtubule depolymerization by Noc increases it. For PCNA, LatB has no effect, while Noc increases accumulation. *N* = number of cells measured for each condition. Error bars show the SEM for each time point. (c) Scheme summarizing the observed results. While perturbation of tubulin (blue) leads to increased XRCC1 and PCNA intensities, perturbation of actin by multiple drugs (red) decreases XRCC1 intensity.

cells expressing a nuclear F/G-actin probe (nuclear GFP-tagged Actin-Chromobody; Plessner *et al.*, 2015). However, the probe was not recruited to the laser line (Supplemental Video S1; Supplemental Figure S1g). Thus, consistent with the lack of Zeocin-induced nuclear actin accumulation, our data do not support a direct action of actin at sites of oxidative damage or BER. Rather,

the reduced recruitment of XRCC1 on actin cytoskeleton perturbation may reflect reduced accessibility to the damage due to impaired activity of actin-containing nucleosome remodelers (Kapoor and Shen, 2014). Alternatively, the nuclear translocation of cofactors of BER may require actin filaments, although for APE1, this does not seem to be the case (Figure 2a).

Perturbation of tubulin increases XRCC1 and PCNA accumulation

Because microtubules are known to influence 53BP1 focus dynamics at uncapped telomeres (Lottersberger *et al.*, 2015) and have been otherwise implicated in repair (Lesca *et al.*, 2005; Poruchynsky *et al.*, 2015), we also examined the effects of microtubule depolymerization on BER factor recruitment to laser-induced damage. Nocodazole (Noc) inhibits tubulin polymerization both in vitro and in vivo (Vasquez *et al.*, 1997) and to our surprise triggered an increase in the rate of recruitment of XRCC1 and PCNA to the laser-induced damage (Figure 4b). XRCC1 accumulated more rapidly on Noc and then was released to a steady-state level by 120 s, while PCNA was both recruited more rapidly and reached a higher plateau on Noc, nearly twice that of the control at 160 s (Figure 4b). In addition, we found that on Noc PCNA spreads laterally and forms foci that persist for at least 30 min, consistent with long-patch BER or other mechanisms of repair that require longer strand synthesis by DNA polymerases (Supplemental Video S2; Figure 4b). The Noc effect on BER factors was unexpected, in particular because it triggered the opposite of actin perturbation (Figure 4, b and c), despite the potential linkage of actin and tubulin filament networks.

LatA increases both nuclear actin and tubulin signals

Given that actin and microtubule perturbation had opposite effects on BER factor accumulation, we examined the impact of both actin and microtubule depolymerization on the localization of the major filament subunits, actin and tubulin. These were monitored by staining with either Rh-phalloidin or anti-tubulin, or else by expressing GFP-tubulin (GFP-TUB1a; gift of J. Chao, FMI) as others have done previously (Rusan *et al.*, 2001; He *et al.*, 2005; Murray and Saint, 2007). First, we confirmed that F-actin nuclear staining increased in the presence of LatA, although this was not observed after treatment with CytB or Noc (Figure 5, a and c). CytB and LatA have different binding sites on actin and distinct modes of action (Low *et al.*, 1975; MacLean-Fletcher and Pollard, 1980; Spector *et al.*, 1989; Wakatsuki *et al.*, 2001), even though both lead to reduced actin polymerization. The differential impact on nuclear actin accumulation suggests that latrunculin binding to G-actin dimers does more than simply depolymerize actin filaments. We next monitored tubulin by antibody staining. Noc triggered depolymerization of microtubules and led to a small increase in the median nuclear:cytoplasmic tubulin ratio as determined by immunostaining (Figure 5, b and d). The treatment with LatA led to a stronger increase (nearly twofold over DMSO). Again, this was not observed with CytB. Whereas the effect was relatively weak as detected by anti-tubulin immunostaining, the tracking of GFP-tubulin in living U2OS cells showed a strong nuclear enrichment of the tagged protein after LatA treatment (5.2-fold increase in the nuclear:cytoplasmic tubulin ratio on LatA; Figure 5, e and f). Using confocal Z-stack imaging, we confirmed that nuclear-localized tubulin has a focal appearance that is present in all planes of the nucleus, ruling out that we are simply observing microtubules collapsed around the nucleus (Figure 5e; Supplemental Figure S2a).

Intrigued by the effect of microtubule depolymerization on BER factor dynamics, we asked whether adding Zeocin to the LatA treatment would enhance or diminish the effect. Scoring the nuclear:cytoplasmic ratio after treatment with LatA ± Zeocin, we see that the increased nuclear localization of tubulin triggered by LatA dropped slightly when Zeocin was added, although only the addition of 100 µg/ml Zeocin with LatA led to a significantly lower enrichment of tubulin in the nucleus (Figure 5, g and h). We conclude that LatA, rather than damage, is the trigger for tubulin relocation to the nucleus, yet tubulin may nonetheless promote BER factor recruitment to damage (Figure 4). We do not know why increased Zeocin reduces the nuclear tubulin signal (Figure 5 h). We note that on Noc, tubulin increases while the phalloidin signal decreases in the nucleus (Figure 5, c and d). This correlates with more efficient recruitment of both XRCC1 and PCNA to laser-induced damage (Figure 4), and suggests that less nuclear actin may be favorable for repair. CytB acts differently from LatA (Figure 5, a–d), as it decreases the nuclear actin signal and has no significant effect on tubulin, suggesting that the specific mode of F-actin perturbation influences both actin and tubulin relocation.

In summary, we find that alteration of cytoplasmic actin and tubulin cytoskeletons alter the accumulation of BER factors at laser-induced DNA damage in opposite ways. Moreover, we find that on LatA treatment both actin and tubulin signals in the nucleus increase. The change in nuclear tubulin levels triggered by LatA treatment correlates with reduced retention or enhanced release of repair factors at the lesion. We do not know whether the role of actin and tubulin on repair factors is direct or indirect, but since we were unable to detect actin recruitment to laser-induced damage, we think that indirect effects on repair factor/cofactor import or recruitment are more likely.

Related evidence for a positive role of Noc in repair and cell proliferation comes from colorectal cancer cells (HCT-116). In an assay of cell proliferation, HCT116 cells showed a negative synergy between CytD and Zeocin, while Noc showed the opposite effect in combination with Zeocin, suppressing toxicity (Hurst *et al.*, unpublished data). This reinforces the positive effect Noc had on XRCC1 recruitment. An earlier study (Akoumianaki *et al.*, 2009) documented the trafficking of tubulin to the nucleus, its nuclear accumulation on Noc, and its ability to alter the interaction of histone H3 with other nuclear proteins. It was also reported that γ-tubulin interacts with Rad51 (Lesca *et al.*, 2005), and that ATM, ATR, DNA-PK, MRN, p53, and 53BP1 all colocalize with cytoplasmic microtubules in the presence of vincristine, an inhibitor of microtubule turnover (Poruchynsky *et al.*, 2015). Thus, the unexpected impact of LatA on tubulin may indirectly alter the abundance or accessibility of damage to repair factors. Noc, on the other hand, appears to have the opposite effect, arguing for a positive role of microtubule depolymerization in BER.

An alternative interpretation of the Noc effect comes from a study of telomeric chromatin mobility and uncapping in fibroblasts (MEFs). These authors found that intact microtubules were required for the mobility of uncapped telomeric ends, while actin filament integrity was not (Lottersberger *et al.*, 2015). The inhibition of microtubule polymerization by Noc, as well as stabilization of microtubules with Taxol, led to decreased dynamics of dysfunctional telomeres. This suggested that microtubule dynamics drive uncapped telomeric chromatin movement, which helps reduce end-to-end fusion (Lottersberger *et al.*, 2015). With respect to our findings, one might suggest that following laser irradiation, microtubule disruption reduces chromatin mobility, favoring the formation of repair foci or repair factor recruitment. Reduced movement of damage undergoing repair has been documented in yeast, whereas the initial response to double-strand breaks is increased movement (reviewed in Seeber *et al.*, 2013).

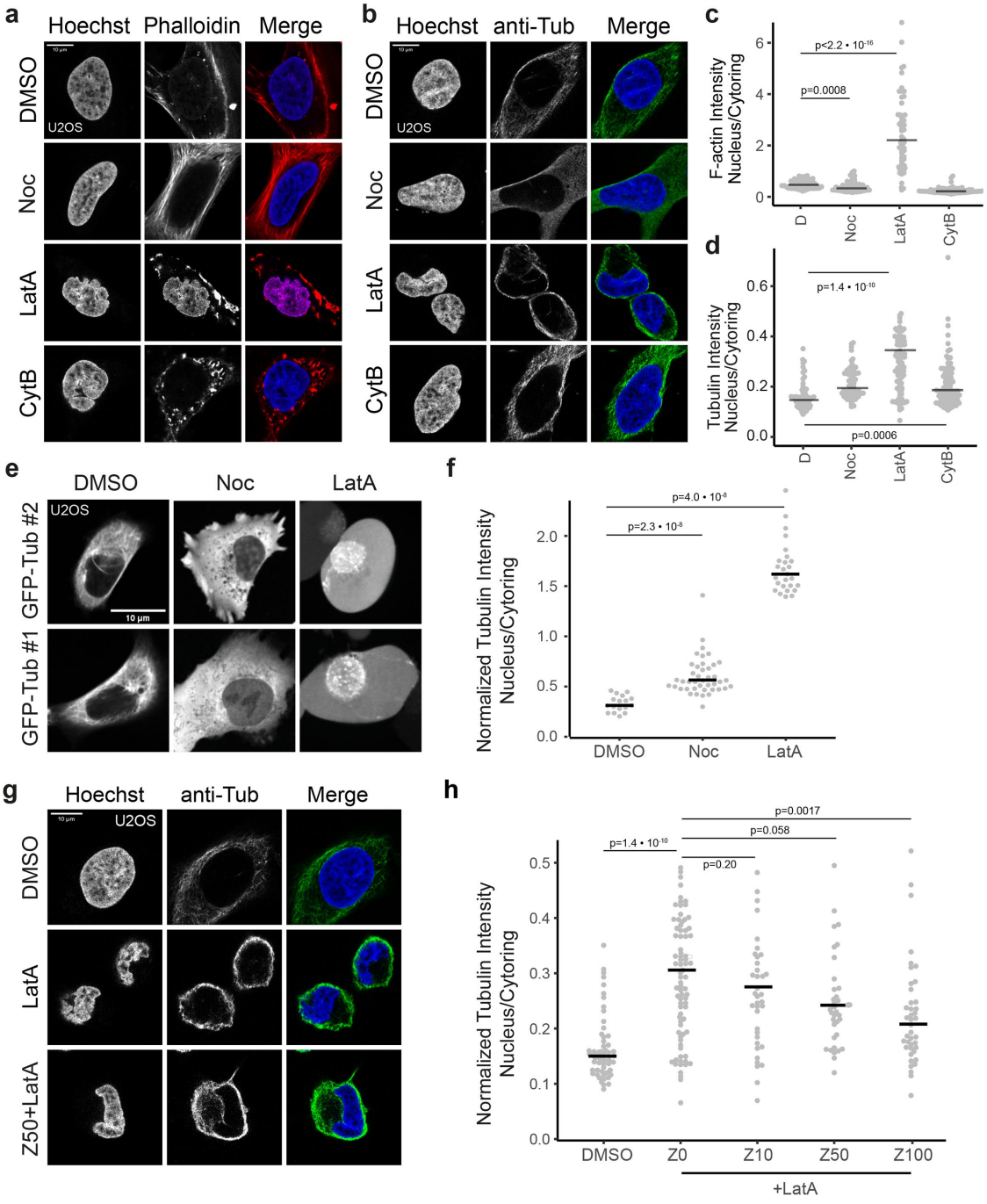

FIGURE 5: LatA causes a cytoplasm to nucleus shift of both actin and tubulin. (a) U2OS cells were treated with 300 nM LatA, 6 µM CytB, or 330 nM Noc for 45 min. Cells were then fixed and stained with Hoechst (nucleus, blue) and Rh-phalloidin (F-actin, red) prior to confocal image acquisition. Images shown are the central plane of the acquired image Z-stack. Scale bar = 10 µm. (b) U2OS cells were treated as in panel a, fixed, and stained with Hoechst (nucleus, blue) and an anti-tubulin antibody (green) prior to confocal image acquisition. Images shown are the central plane of the acquired image Z-stack. Scale bar = 10 µm. (c) Quantitation of the image data set of which selected examples are shown in panel a. Each dot represents the nucleus/cytoring intensity ratio in one cell ($N \geq 57$ per condition) in the red channel (Rh-phalloidin). D = DMSO control. Horizontal bars indicate median values. Columns were compared with Wilcoxon rank sum test in R and relevant p values are indicated. For CytB vs. DMSO, $p = 1.19 \times 10^{-15}$. (d) As in c but for the image data set for which samples are shown in b. Each dot represents the nucleus/cytoring intensity ratio per cell ($N \geq 57$ per condition) in the green channel (tubulin). D = DMSO. Horizontal bars indicate median values. Columns were compared with a Wilcoxon rank sum test in R and relevant p values are indicated. For Noc vs. DMSO, $p = 3.58 \times 10^{-7}$. (e) U2OS cells expressing GFP-tubulin from a plasmid were treated with DMSO, 300 nM LatA, or 330 nM Noc at the onset of live cell microscopy. Images were acquired after 10–20 min. The figure shows MIPs of 1–3 middle planes of an image Z-stack. See Supplemental Figure S2 for a series of focal planes. Scale bar = 10 µm. (f) Quantitation of the image data set of which selected examples are shown in e. Each dot represents the nucleus/cytoplasm intensity ratio per cell

The fact that LatA is detrimental to cell survival of Zeocin-induced damage could reflect a variety of events. First, we note that nuclear tubulin levels increase significantly in some cell types. The exact impact of this is still unknown. Second, nuclear actin levels increase on LatA, potentially inhibiting chromatin remodeler function, as discussed elsewhere (Seeber *et al.*, 2013; Hurst *et al.*, 2019, unpublished data). Third, there appears to be cross-talk between actin and tubulin that has not been highlighted in past studies of DNA repair. Our work sheds light on a potential side effect of latrunculin, which binds at the interface between two actin monomers to alter their homodimerization site (Morton *et al.*, 2000). Latrunculin may not only alter actin polymerization but also affect microtubule stability. While we have no clear mechanism for this effect, the potential impact of actin depolymerizing drugs on microtubules should be taken into consideration when latrunculin is used in cell-based assays. This may be particularly important in the context of BER (Nichols and Sancar, 1992; Umar *et al.*, 1996; Beard *et al.*, 2019), because cell proliferation in colorectal cancer cells following Zeocin-induced damage is decreased by inhibiting actin polymerization and is increased by Noc (Hurst *et al.*, unpublished data). Whereas assays of viability are based on a prolonged incubation with the drugs over several days, they are consistent with a scenario in which Noc favors rapid repair factor recruitment to sites of damage. Future studies will address the role of tubulin in BER as well as its interplay with actin in repair more generally.

MATERIALS AND METHODS

Request a protocol through *Bio-protocol*.

Cell culture

Native HeLa and U2OS cells and U2OS/Cos7 cells stably expressing XRCC1-GFP/APE1-GFP (gifts from P. Schaer, Department of Biomedicine, University of Basel) were cultured in DMEM containing 10% fetal calf serum (FCS) under standard conditions. HeLa or U2OS cells were transfected with expression plasmids with Lipofectamine (Lipofectamine 2000, Invitrogen) according to the manufacturer's recommendations. We obtained the GFP-PCNA plasmid from P. Schaer (Department of Biomedicine, University of Basel), the GFP-tubulin plasmid from Jeffrey Chao (FMI, Basel), and purchased the plasmids encoding nuclear actin probes from Addgene (#58469 RPEL1-EN, #58466 Utr230-EN, #58468 EN) and Chromotek [#acgn, Nuclear Actin-Chromobody plasmid (TagGFP2)]. Prior to the experiment, GFP expression levels were checked by microcopy.

For live cell microscopy, cells were seeded into imaging chambers (chambered µ-Slide 4 Well, ibidi). To avoid additional fluorescence, DMEM containing a dye for pH indication and 10% FCS was exchanged with color-free DMEM medium containing 1% FCS. Cells were treated with 10 µM Olaparib (SelleckChem, S1060), 20–60 nM LatB (Abcam, ab144291), 300 nM LatA (Focus Biomolecules, FB1150), 0.5 µM Jasp (Santa Cruz Biotechnology), 6 µM CytB (Sigma, C6762), 330 nM Noc (Sigma, M1404), or their solvent 30 min prior to imaging and were kept at 37°C in an incubation chamber on top of the microscope during the imaging procedure.

For postfixation staining with phalloidin and immunostaining with anti-tubulin, native U2OS cells were treated with DMSO, 300 nM LatA, 6 µM CytB, or 330 nM Noc for 45 min. For staining of primary human fibroblasts (HDFn, Life Technologies), cells were cultured in Medium 106 with Low Serum Growth Supplement Kit (Life Technologies) supplemented with SiR-actin (2 mM) to visualize actin, then treated with LatB (300 nM), Zeocin (15 µg/ml), or a combination of the two for 1 h.

APE1, tubulin, and F-actin staining

For APE1 immunostaining, HeLa cells were fixed with 4% freshly dissolved paraformaldehyde in phosphate-buffered saline (PFA/PBS) at room temperature (RT) for 30 min and permeabilized with 0.1% Triton-X100 at RT for 2 min. After 1 h blocking at RT in 1% bovine serum albumin (BSA) in PBS, cells were exposed to the primary antibody (APE1, Gentex GTX110558, 1:100) overnight at 4°C. Cells were washed with PBS (3 × 20 min, RT) and incubated with the secondary antibody (Alexa-488 Invitrogen, 1:2000 in 1% BSA, RT in the dark for 1 h). Again, cells were washed with PBS and incubated with DAPI (Sigma, D9542) and Rh-phalloidin (Invitrogen, R415), according to the manufacturer's instructions (1 h, RT), and were washed again prior to mounting with antifade (ProLong Gold, Invitrogen, P36934).

For the F-actin staining, U2OS cells were fixed with 4% PFA/PBS for 30 min at 25°C (RT). Cells were permeabilized with 0.1% Triton-X100/PBS for 2 min at RT and incubated with Rh-phalloidin (Invitrogen, R415) overnight at 4°C according to the manufacturer's recommendation. Then, cells were washed 3× with PBS for 20 min, and Hoechst (Invitrogen R37605) was added during the last wash.

For the tubulin immunostaining, U2OS cells were fixed with 4% PFA/PBS for 30 min at 25°C (RT). Cells were permeabilized with 0.1% Triton X-100/PBS for 2 min at RT and blocked with 1% BSA/PBS for 1 h at RT prior to overnight incubation with the tubulin antibody in 1% BSA/PBS at 4°C (Thermo Fisher Scientific, MA1-80017, 1:500). Then, cells were washed 3× with PBS for 20 min and incubated with the secondary antibody in the dark for 1 h (Invitrogen #A32723 anti-mouse, 1:2000 in 1% BSA/PBS). Cells were washed 3× with PBS for 20 min and Hoechst (Invitrogen R37605) was added during the last wash.

Western blotting

HeLa and U2OS cells were cultured in multi-well dishes as described above and treated with Zeocin and/or LatB or LatA at the concentration and duration indicated in each figure legend. After removal of the cell culture medium, 100 µl 1.5× SDS sample buffer

($N \geq 26$ per condition) in the green channel (tubulin). Per pixel intensity values for the nuclear/cytoplasmic GFP-tubulin ratio were obtained by manual quantitation middle plane MIPs with ImageJ. The average pixel intensity value within a defined nuclear area was divided by the average pixel value within a cytoplasmic area of the same size. Horizontal bars indicate median values and columns were compared by the Wilcoxon rank sum test in R and relevant *p* values are indicated. (g) U2OS cells were treated with DMSO, 300 nM LatA, or a combination of 300 nM LatA plus 10, 50, 100, or 200 µg/ml Zeocin for 45 min. Cells were fixed and stained with Hoechst (nucleus, blue) and an anti-tubulin antibody (green) prior to confocal image acquisition. Images shown are the central plane of the acquired image Z-stack. See Supplemental Figure S2 for through focal series. Scale bar = 10 µm. (h) Quantitation of the image data set of which selected examples are shown in g. Each dot represents the nucleus/cytoring intensity ratio per cell ($N \geq 34$ per condition) in the green channel (tubulin). Bars indicate median values and columns were compared by the Wilcoxon rank sum test in R and relevant *p* values are indicated.

was added, cells were scraped from the dish in the buffer, and the lysate was boiled for 10 min at 90°C and sonicated to decrease sample viscosity (2 × 3 s, low level). Proteins were separated by SDS–PAGE (NuPAGE, Bis-Tris, 4–12% gradient gel, 1× MES running buffer) and transferred to a PVDF membrane in a semidry manner (Trans-Blot Turbo Transfer System, Bio-Rad). After blocking [5% milk in TEN-T (10 mM Tris-Cl, 1 mM EDTA, 100 mM NaCl and 0.05% Tween-20), 1 h at RT], the membrane was incubated with primary antibodies [Tubulin (ab4074, abcam), γH2AX (JBW301 Millipore, 1:2000), ERK2 (Cell Signaling)] at 4°C overnight. After washing (TEN-T buffer 3 × 20 min at RT), horseradish peroxidase (HRP)-coupled secondary antibodies (1 h at RT, 3 × 20 min washing with TEN-T) were used to detect the primary antibodies with an HRP substrate (ECL, Amersham).

Image acquisition

DNA damage was induced with a VisiFRAP module (Visitron) mounted on the backport of the microscope and equipped with a 405-nm laser (Toptica, illumination power at the objective 12.8 mW, ≥1 ms/pixel). Spinning-disk confocal images were acquired with an Olympus IX81 microscope equipped with a UPlanSApo 20×/0.85 or a PlanApo 100×/1.45 TIRFM oil objective, a CSU-X1 scan-head (Yokogawa), an Evolve 512 EMCCD camera (Photometrics), and a ASI MS-2000 Z-piezo stage. Fluorophores were excited at 405 nm (DAPI, Hoechst), 488 nm (GFP), and 561 nm (RFP), and emitted fluorescence was acquired on separate cameras (AHF LED400-405 HC filter for DAPI, Semrock FF02-525/40–25 filter for GFP, Semrock FF01-617/73-25 filter for RFP). For live cell microscopy, a time course of images was acquired for a period of 2–3 min with 100- to 500-ms intervals. For acquisition of stained fixed cells, HeLa cell staining, Cos7 cells, and Z-stacks of confocal images were acquired with the same lasers and filter sets. Confocal images of fixed, and stained U2OS cells (Hoechst, anti-tubulin, Rh-phalloidin) were acquired with an Inverted DMi8 S microscope (Leica) at 63× magnification.

Image analysis

Fluorescence recovery after photobleaching (FRAP) time series were analyzed in ImageJ with a modified standard script (https://imagej.net/Analyze_FRAP_movies_with_a_Jython_script). For FRAP analysis, the intensity prior to bleaching, determined during 3–5 confocal image acquisitions before laser exposure, is set to 1. Instead of measuring the recovery to the initial intensity, the modified script allows intensity increases up to any value. After setting the intensity prior to bleaching/laser exposure to 1, the script normalizes the nuclear intensity of a field on the laser line to the intensity of a field of equal area outside the laser line for every image, generating normalized intensity values on the laser line for each time point. Cells that changed their location during the acquisition were manually excluded from the analysis. Values were plotted with GraphPad Prism 8.4.3.

For quantitation of nuclear APE1 intensity, a CellProfiler pipeline was created. Nuclei were identified with DAPI (blue). Average nuclear APE1 intensities were calculated from image Z-stack average projections in the green channel inside the DAPI mask (nucleus). The values in the graph are average nuclear pixel intensities. The minimum number of nuclei is indicated in the figure legends.

The nuclear cytoplasmic GFP-tubulin ratio in U2OS cells was calculated with ImageJ software as a fraction of the average pixel intensity within a manually drawn box inside the nucleus over the average pixel intensity within a box of the same size in the cytoplasm. The images used for quantitation are average intensity projections of the nuclear middle plane plus the planes below and above (3 planes in total).

The Nucleus/Cytoring intensity ratios for IF and Rh-phalloidin stained U2OS cell image stacks were calculated as follows. Image stacks covering 3–10 cells per field of view were acquired in the red (F-actin) or green (anti-tubulin) plus the blue (Hoechst) channel. Stacks in each channel were split into single-plane images with an ImageJ macro. Using CellProfiler, the total Hoechst area for each plane was calculated and the plane with the maximum Hoechst area (central nuclear plane) was selected for further analysis. With CellProfiler, the average intensity per pixel in either the red or the green channel was determined within the nucleus and within a 10-pixel cytoplasmic ring around the nucleus. The intensity fraction of nucleus/cytoring per cell was calculated and subjected to statistical analysis with GraphPad Prism.

XRCC1 spot counting

XRCC1 spots were counted manually with the ImageJ Cell Counter plugin. Statistical significance was determined as described below.

Statistical analysis

Statistical tests were performed with GraphPad Prism 8.4.3 and with R v4.1.0 (Team, 2021), with comparable results. Normality was assessed with a Shapiro–Wilk test. Then, a Wilcoxon Mann–Whitney test (hereafter called Wilcoxon rank sum test) without continuity correction was used to compare values between conditions. The sample size of the column containing least counts is indicated in the figure legend. A negative binomial regression with the condition as the sole predictor was used to compare the number of XCRR foci between conditions using the glm.nb function from the MASS R package (v7.3-54) (Venables and Ripley, 2011).

ACKNOWLEDGMENTS

We thank Charlotte Soneson of the FMI Computational biology group for invaluable help with statistical analyses and Shota Yamasaki, of the Harata laboratory (Tohoku University, Sendai) for HDFn cell viability assays. We thank Primo Schaer for U2OS cell lines expressing GFP-tagged XRCC1, Cos7 cells expressing GFP-APE1, and the GFP-PCNA expression plasmid; Laurent Gelman and Steven Bourke (FMI FAIM) for help with microscopy; and Jan Eglinger for advice on image analysis. The GFP-tubulin plasmid was a generous gift of Jeff Chao (FMI). We thank Primo Schaer, David Schuermann, and Jan Padeken for feedback on the paper and for valuable discussions. This study was supported by the Swiss National Science Foundation Grant 31003A_176286 to SMG and by the Novartis Research Foundation.

REFERENCES

Akoumianaki T, Kardassis D, Polioudaki H, Georgatos SD, Theodoropoulos PA (2009). Nucleocytoplasmic shuttling of soluble tubulin in mammalian cells. J Cell Sci 122, 1111–1118.

Andrin C, McDonald D, Attwood KM, Rodrigue A, Ghosh S, Mirzayans R, Masson JY, Dellaire G, Hendzel MJ (2012). A requirement for polymerized actin in DNA double-strand break repair. Nucleus 3, 384–395.

Beard WA, Horton JK, Prasad R, Wilson SH (2019). Eukaryotic base excision repair: new approaches shine light on mechanism. Annu Rev Biochem 88, 137–162.

Belin BJ, Lee T, Mullins RD (2015). Correction: DNA damage induces nuclear actin filament assembly by Formin-2 and Spire-1/2 that promotes efficient DNA repair. Elife 4, 07735.

Caridi CP, D'Agostino C, Ryu T, Zapotoczny G, Delabaere L, Li X, Khodaverdian VY, Amaral N, Lin E, Rau AR, Chiolo I (2018). Nuclear F-actin and myosins drive relocalization of heterochromatic breaks. Nature 559, 54–60.

Caridi CP, Plessner M, Grosse R, Chiolo I (2019). Nuclear actin filaments in DNA repair dynamics. Nat Cell Biol 21, 1068–1077.

Chang W, Worman HJ, Gundersen GG (2015). Accessorizing and anchoring the LINC complex for multifunctionality. J Cell Biol 208, 11–22.

Chattopadhyay R, Wiederhold L, Szczesny B, Boldogh I, Hazra TK, Izumi T, Mitra S (2006). Identification and characterization of mitochondrial abasic (AP)-endonuclease in mammalian cells. Nucleic Acids Res 34, 2067–2076.
Dianov GL, Hubscher U (2013). Mammalian base excision repair: the forgotten archangel. Nucleic Acids Res 41, 3483–3490.
Dopie J, Skarp KP, Rajakyla EK, Tanhuanpaa K, Vartiainen MK (2012). Active maintenance of nuclear actin by importin 9 supports transcription. Proc Natl Acad Sci USA 109, E544–E552.
Du J, Fan YL, Chen TL, Feng XQ (2015). Lifeact and Utr230 induce distinct actin assemblies in cell nuclei. Cytoskeleton (Hoboken) 72, 570–575.
Endutkin AV, Yudkina AV, Sidorenko VS, Zharkov DO (2019). Transient protein-protein complexes in base excision repair. J Biomol Struct Dyn 37, 4407–4418.
Galkin VE, Orlova A, VanLoock MS, Rybakova IN, Ervasti JM, Egelman EH (2002). The utrophin actin-binding domain binds F-actin in two different modes: implications for the spectrin superfamily of proteins. J Cell Biol 157, 243–251.
Godon C, Cordelieres FP, Biard D, Giocanti N, Megnin-Chanet F, Hall J, Favaudon V (2008). PARP inhibition versus PARP-1 silencing: different outcomes in terms of single-strand break repair and radiation susceptibility. Nucleic Acids Res 36, 4454–4464.
He Y, Francis F, Myers KA, Yu W, Black MM, Baas PW (2005). Role of cytoplasmic dynein in the axonal transport of microtubules and neurofilaments. J Cell Biol 168, 697–703.
Hendzel MJ (2014). The F-act's of nuclear actin. Curr Opin Cell Biol 28, 84–89.
Holzinger A (2009). Jasplakinolide: an actin-specific reagent that promotes actin polymerization. Methods Mol Biol 586, 71–87.
Howard MJ, Wilson SH (2018). DNA scanning by base excision repair enzymes and implications for pathway coordination. DNA Repair (Amst) 71, 101–107.
Hurst V, Shimada K, Gasser SM (2019). Nuclear actin and actin-binding proteins in DNA repair. Trends Cell Biol 29, 462–476.
Kapoor P, Shen X (2014). Mechanisms of nuclear actin in chromatin-remodeling complexes. Trends Cell Biol 24, 238–246.
Kim DI, Birendra KC, Roux KJ (2015). Making the LINC: SUN and KASH protein interactions. Biol Chem 396, 295–310.
Krokan HE, Bjoras M (2013). Base excision repair. Cold Spring Harb Perspect Biol 5, a012583.
Lesca C, Germanier M, Raynaud-Messina B, Pichereaux C, Etievant C, Emond S, Burlet-Schiltz O, Monsarrat B, Wright M, Defais M (2005). DNA damage induce gamma-tubulin-RAD51 nuclear complexes in mammalian cells. Oncogene 24, 5165–5172.
Lindahl T (1993). Instability and decay of the primary structure of DNA. Nature 362, 709–715.
Lottersberger F, Karssemeijer RA, Dimitrova N, de Lange T (2015). 53BP1 and the LINC complex promote microtubule-dependent DSB mobility and DNA repair. Cell 163, 880–893.
Low I, Dancker P, Wieland T (1975). Stabilization of F-actin by phalloidin. Reversal of the destabilizing effect of cytochalasin B. FEBS Lett 54, 263–265.
MacLean-Fletcher S, Pollard TD (1980). Mechanism of action of cytochalasin B on actin. Cell 20, 329–341.
Miura M (1999). Detection of chromatin-bound PCNA in mammalian cells and its use to study DNA excision repair. J Radiat Res 40, 1–12.
Mohan R, John A (2015). Microtubule-associated proteins as direct cross-linkers of actin filaments and microtubules. IUBMB Life 67, 395–403.
Moor NA, Lavrik OI (2018). Protein-protein interactions in DNA base excision repair. Biochemistry (Mosc) 83, 411–422.
Moores CA, Kendrick-Jones J (2000). Biochemical characterisation of the actin-binding properties of utrophin. Cell Motil Cytoskeleton 46, 116–128.
Morton WM, Ayscough KR, McLaughlin PJ (2000). Latrunculin alters the actin-monomer subunit interface to prevent polymerization. Nat Cell Biol 2, 376–378.
Murray MJ, Saint R (2007). Photoactivatable GFP resolves Drosophila mesoderm migration behaviour. Development 134, 3975–3983.
Muster B, Rapp A, Cardoso MC (2017). Systematic analysis of DNA damage induction and DNA repair pathway activation by continuous wave visible light laser micro-irradiation. AIMS Genet 4, 47–68.
Nichols AF, Sancar A (1992). Purification of PCNA as a nucleotide excision repair protein. Nucleic Acids Res 20, 2441–2446.
Pimm ML, Henty-Ridilla JL (2021). New twists in actin-microtubule interactions. Mol Biol Cell 32, 211-217.
Plessner M, Melak M, Chinchilla P, Baarlink C, Grosse R (2015). Nuclear F-actin formation and reorganization upon cell spreading. J Biol Chem 290, 11209–11216.
Pollard TD, Goldman RD (2018). Overview of the Cytoskeleton from an Evolutionary Perspective. Cold Spring Harb Perspect Biol 10, a030288.
Poruchynsky MS, Komlodi-Pasztor E, Trostel S, Wilkerson J, Regairaz M, Pommier Y, Zhang X, Kumar Maity T, Robey R, Burotto M, *et al.* (2015). Microtubule-targeting agents augment the toxicity of DNA-damaging agents by disrupting intracellular trafficking of DNA repair proteins. Proc Natl Acad Sci USA 112, 1571–1576.
Povirk LF (1996). DNA damage and mutagenesis by radiomimetic DNA-cleaving agents: bleomycin, neocarzinostatin and other enediynes. Mutat Res 355, 71–89.
Rusan NM, Fagerstrom CJ, Yvon AM, Wadsworth P (2001). Cell cycle-dependent changes in microtubule dynamics in living cells expressing green fluorescent protein-alpha tubulin. Mol Biol Cell 12, 971–980.
Schrank BR, Aparicio T, Li Y, Chang W, Chait BT, Gundersen GG, Gottesman ME, Gautier J (2018). Nuclear ARP2/3 drives DNA break clustering for homology-directed repair. Nature 559, 61–66.
Schuermann D, Ziemann C, Barekati Z, Capstick M, Oertel A, Focke F, Murbach M, Kuster N, Dasenbrock C, Schar P (2020). Assessment of genotoxicity in human cells exposed to modulated electromagnetic fields of wireless communication devices. Genes (Basel) 11, 347.
Schwarzerova K, Bellinvia E, Martinek J, Sikorova L, Dostal V, Libusova L, Bokvaj P, Fischer L, Schmit AC, Nick P (2019). Tubulin is actively exported from the nucleus through the Exportin1/CRM1 pathway. Sci Rep 9, 5725.
Seeber A, Hauer M, Gasser SM (2013). Nucleosome remodelers in double-strand break repair. Curr Opin Genet Dev 23, 174–184.
Serebryannyy LA, Yuen M, Parilla M, Cooper ST, de Lanerolle P (2016). The effects of disease models of nuclear actin polymerization on the nucleus. Front Physiol 7, 454. doi: 10.3389/fphys.2016.00454.
Shimada K, Filipuzzi I, Stahl M, Helliwell SB, Studer C, Hoepfner D, Seeber A, Loewith R, Movva NR, Gasser SM (2013). TORC2 signaling pathway guarantees genome stability in the face of DNA strand breaks. Mol Cell 51, 829–839.
Shimada K, van Loon B, Gerhold CB, Bregenhorn S, Hurst V, Roth G, Tarashev C, Heinis C, Jiricny J, Gasser SM (2020). Uncoordinated long-patch base excision repair at juxtaposed DNA lesions generates a lethal accumulation of double-strand breaks. bioRxiv 2020.2011.2015.383513.
Spector I, Shochet NR, Blasberger D, Kashman Y (1989). Latrunculins—novel marine macrolides that disrupt microfilament organization and affect cell growth: I. Comparison with cytochalasin D. Cell Motil Cytoskeleton 13, 127–144.
Steinacher R, Barekati Z, Botev P, Kusnierczyk A, Slupphaug G, Schar P (2019). SUMOylation coordinates BERosome assembly in active DNA demethylation during cell differentiation. EMBO J 38, e99242.
Stuven T, Hartmann E, Gorlich D (2003). Exportin 6: a novel nuclear export receptor that is specific for profilin.actin complexes. EMBO J 22, 5928–5940.
Team RC (2021). R: A Language and Environment for Statistical Computing. R Foundation for Statistical Computing, Vienna, Austria.
Umar A, Buermeyer AB, Simon JA, Thomas DC, Clark AB, Liskay RM, Kunkel TA (1996). Requirement for PCNA in DNA mismatch repair at a step preceding DNA resynthesis. Cell 87, 65–73.
Vasquez RJ, Howell B, Yvon AM, Wadsworth P, Cassimeris L (1997). Nanomolar concentrations of nocodazole alter microtubule dynamic instability in vivo and in vitro. Mol Biol Cell 8, 973–985.
Venables WN, Ripley BD (2011). Modern applied statistics with S. Springer, New York; London.
Visegrady B, Lorinczy D, Hild G, Somogyi B, Nyitrai M (2005). A simple model for the cooperative stabilisation of actin filaments by phalloidin and jasplakinolide. FEBS Lett 579, 6–10.
Wakatsuki T, Schwab B, Thompson NC, Elson EL (2001). Effects of cytochalasin D and latrunculin B on mechanical properties of cells. J Cell Sci 114, 1025–1036.
Walss-Bass C, Xu K, David S, Fellous A, Luduena RF (2002). Occurrence of nuclear beta(II)-tubulin in cultured cells. Cell Tissue Res 308, 215–223.
Wei M, Fan X, Ding M, Li R, Shao S, Hou Y, Meng S, Tang F, Li C, Sun Y (2020). Nuclear actin regulates inducible transcription by enhancing RNA polymerase II clustering. Sci Adv 6, eaay6515.